

P. Jacquet, L. Colas, M.-L. Mayoral, G. Arnoux, V. Bobkov, M. Brix, A. Czarnecka, D. Dodt, F. Durodie, A. Ekedahl, D. Frigione M. Fursdon, E. Gauthier, M. Goniche, M. Graham, E. Joffrin, A. Korotkov, E. Lerche, J. Mailloux, I. Monakhov, J. Ongena, V. Petrzilka, F. Rimini, A. Sirinelli, C. Portafaix, V. Riccardo, Z. Vizvary, K.-D. Zastrow and JET EFDA contributors

# Heat-Loads on JET Plasma Facing Components from ICRF and LH Wave Absorption in the Scrape-Off-Layer

“This document is intended for publication in the open literature. It is made available on the understanding that it may not be further circulated and extracts or references may not be published prior to publication of the original when applicable, or without the consent of the Publications Officer, EFDA, Culham Science Centre, Abingdon, Oxon, OX14 3DB, UK.”

“Enquiries about Copyright and reproduction should be addressed to the Publications Officer, EFDA, Culham Science Centre, Abingdon, Oxon, OX14 3DB, UK.”

The contents of this preprint and all other JET EFDA Preprints and Conference Papers are available to view online free at [www.iop.org/Jet](http://www.iop.org/Jet). This site has full search facilities and e-mail alert options. The diagrams contained within the PDFs on this site are hyperlinked from the year 1996 onwards.

# Heat-Loads on JET Plasma Facing Components from ICRF and LH Wave Absorption in the Scrape-Off-Layer

P. Jacquet<sup>1</sup>, L. Colas<sup>2</sup>, M.-L. Mayoral<sup>1</sup>, G. Arnoux<sup>1</sup>, V. Bobkov<sup>3</sup>, M. Brix<sup>1</sup>, A. Czarnecka<sup>4</sup>, D. Dodt<sup>3</sup>, F. Durodie<sup>5</sup>, A. Ekedahl<sup>2</sup>, D. Frigione<sup>6</sup>, M. Fursdon<sup>1</sup>, E. Gauthier<sup>2</sup>, M. Goniche<sup>2</sup>, M. Graham<sup>1</sup>, E. Joffrin<sup>2</sup>, A. Korotkov<sup>1</sup>, E. Lerche<sup>5</sup>, J. Mailloux<sup>1</sup>, I. Monakhov<sup>1</sup>, J. Ongena<sup>5</sup>, V. Petržilka<sup>7</sup>, F. Rimini<sup>8</sup>, A. Sirinelli<sup>1</sup>, C. Portafaix<sup>2</sup>, V. Riccardo<sup>1</sup>, Z. Vizvary<sup>1</sup>, K.-D. Zastrow<sup>1</sup> and JET EFDA contributors\*

*JET-EFDA, Culham Science Centre, OX14 3DB, Abingdon, UK*

<sup>1</sup>*EURATOM-CCFE Fusion Association, Culham Science Centre, OX14 3DB, Abingdon, OXON, UK*

<sup>2</sup>*CEA, IRFM, F-13108 Saint Paul-lez-Durance, France*

<sup>3</sup>*Max-Planck-Institut für Plasmaphysik, EURATOM-Assoziation, Garching, Germany*

<sup>4</sup>*Association Euratom-IPPLM, Hery 23, 01-497 Warsaw, Poland*

<sup>5</sup>*Association EURATOM-Belgian State, Department of Applied Physics Ghent University, B-9000 Ghent, Belgium*

<sup>6</sup>*EURATOM-ENEA sulla Fusione, C.R. Frascati, Roma, Italy*

<sup>7</sup>*Association EURATOM-IPP.CR, Za Slovankou 3, 182 21 Praha 8, Czech Republic*

<sup>8</sup>*EFDA-CSU, Culham Science Centre, OX14 3DB, Abingdon, OXON, UK*

\* *See annex of F. Romanelli et al, "Overview of JET Results", (23rd IAEA Fusion Energy Conference, Daejeon, Republic of Korea (2010)).*

Preprint of Paper to be submitted for publication in Proceedings of the  
23rd IAEA Fusion Energy Conference, Daejeon, Republic of Korea  
(10th October 2010 - 16th October 2010)



## **ABSTRACT:**

In JET, Lower Hybrid (LH) and Ion Cyclotron Resonance Frequency (ICRF) wave absorption in the Scrape-Off Layer (SOL) can lead to enhanced heat fluxes on some Plasma Facing Components (PFCs). When using ICRF, hot spots are observed on the antenna structures and on limiters close to the powered antennae and are explained by acceleration of particles in RF-rectified sheath potentials. High temperatures up to 800°C can be reached on locations where a deposit has built up on tile surfaces. Modelling taking into account the fast thermal response of deposit layers can well reproduce surface temperature measurements via IR imaging, and allow evaluation of the heat fluxes local to active ICRF antennae. The flux scales linearly with the SOL density and with the antenna voltage. Strap phasing corresponding to wave spectra with lower  $k_{\parallel}$  values can lead to a significant increase of hot spot intensity in agreement with antenna modelling that predicts, in that case, an increase of RF sheath rectification. LH absorption in front of the antenna through Electron Landau Damping of the wave with high  $N_{\parallel}$  components generates hot spots precisely located on PFCs magnetically connected to the launcher. Analysis of LH hot spot surface temperature from IR measurements allows quantification of the power flux along the field lines: in worst case scenarios it is in the range of 15-30MW/m<sup>2</sup>. The main driving parameter is the LH power density along the horizontal rows of the launcher, the heat fluxes scaling roughly with the square of LH power density. The ionisation of neutrals in the SOL by LH power plays an important role in the absorption mechanism and far SOL density enhancement.

## **1. INTRODUCTION**

When using ICRF or LH systems on JET, parasitic wave absorption in the SOL can lead, for the ICRF case, to enhanced impurity release [1] and to enhanced heat fluxes on some PFCs [2][3]. Relatively modest parallel power densities can be an issue in the far SOL because the field lines may not be at grazing incidence on targets. These heat loads have not been an operational issue with the carbon wall, but from 2011 JET will operate with a new ITER-like wall consisting mainly of Beryllium (Be) tiles in the chamber and tungsten tiles in the divertor area [4]. As the heat fluxes tolerated by Be tiles before melting are much lower than for Carbon Fibre reinforced Carbon (CFC) tiles, experiments were carried-out in 2008-2009 to better characterise these phenomena, and determine their driving parameters. This work relied on measurements from a wide angle Infra-Red (IR) camera [5] viewing the ICRF A2 antennae A and B (JET ICRF A2 antenna system is described in [6]), the ICRF ITER-Like Antenna (ILA), the lower divertor region, and the upper dump plate region (see FIG. 1). The interaction between ICRF antennae and the plasma SOL can lead to hot spots on the A2 antenna septa, and on the poloidal limiters in the vicinity of the antennae. LH hot spots can develop on some of the objects viewed by the camera, when intercepting fast electron beams generated from the interaction of the LH waves with the plasma in front of the launcher [7]. The time resolution of the camera is typically ~ 16ms, and its spatial resolution is ~3.5cm.

## **2. IR MEASUREMENTS ANALYSIS METHOD.**

It is important to analyse the surface temperature measurements of PFCs so as to determine the heat flux to which these components are subjected. Heat flux evaluation from temperature measurements is an inverse heat conduction problem, and depending on details in material properties, geometry and boundary conditions, a wide range of heat fluxes can lead to the same surface temperature response [8]. Assumptions associated with different models need to be carefully evaluated because they can lead to huge differences in the evaluated heatfluxes whilst still giving a good explanation of the measured surface temperature. The deconvolution of surface temperature measurement to evaluate the heat fluxes as a function of time is adapted from [8]. We assume that the thermal system is linear (this assumption holds if flux variations are not too large) and that the thermal response does not evolve over time. We define the heat load at one location by  $Q(t)$ .  $Q(t)$  is typically a maximum or an averaged heat flux over the heat pattern. In order to fully characterize  $Q(t)$ , one needs to follow the time trace of the surface temperature  $T(t)$  (typically the maximum temperature of a hot spot, or spatially averaged over a hot zone). For  $(t < t_0)$  it is assumed that the applied flux is null and the object temperature is  $T_0$ . The thermal load is sliced into  $N$  time sequences with  $N$  constant fluxes  $Q_i$ ,  $i = 1$  to  $N$ ; between  $t_{i-1}$  and  $t_i$ , the applied heat flux is  $Q_i = \sum_{j=1}^i \Delta Q_j$ . We define  $F(t)$  as the thermal response of the object to be analysed to a reference Heaviside excitation applied from  $t=0$  (flux is null before  $t=0$  and equal to a reference power density afterwards). Ideally

$F(t)$  should be measured in controlled conditions. In our case, it is derived from thermal simulations (response to a heat step). The temperature  $T_i$  at the end of sequence  $i$  is then:

$$T_i = T_i - T_0 = \sum_{j=1}^i \Delta Q_j F(t_i - t_{j-1})$$

Then calculating the flux increments  $Q_j$  is just a matter of matrix inversion

$$\Delta \mathbf{Q} = \mathbf{M}^{-1} \Delta \mathbf{T} = \mathbf{M}^{-1} \Delta \mathbf{T}_{\text{IR}}, \text{ where}$$

$$\Delta \mathbf{Q} = \begin{bmatrix} \Delta Q_1 \\ \Delta Q_2 \\ \dots \\ \Delta Q_N \end{bmatrix} ; \Delta \mathbf{T} = \begin{bmatrix} \Delta T_1 \\ \Delta T_2 \\ \dots \\ \Delta T_N \end{bmatrix} ; \text{ and } \mathbf{M} = \begin{bmatrix} F(t_1 - t_0) & 0 & \dots & 0 \\ F(t_2 - t_0) & F(t_2 - t_1) & \dots & 0 \\ \dots & \dots & \dots & \dots \\ F(t_1 - t_0) & F(t_N - t_1) & \dots & F(t_N - t_{N-1}) \end{bmatrix}$$

$\Delta T_{\text{IR}}$  corresponds to surface temperature increase as measured by the IR camera. Finally, we notice that we have taken into account the temperature dependent thermal properties of the tile material: tiles were modelled with ANSYS<sup>TM</sup> [12], with the ‘non linear’ thermal properties of the material. The heat-fluxes applied in the reference simulations to calculate  $F(t)$  are of the same order of magnitude as the heat fluxes we want to evaluate, and the start temperature  $T_0$  matches the measurements.

### 3. HOT SPOTS ON PFCS SURROUNDING ICRF ANTENNAE WHEN LOCAL ICRF IS USED.

When using ICRF waves, hot spots are observed on the antennae structure and on limiters close

to the powered antennae, which can be explained by enhanced heat loads due to acceleration of particles in RF-rectified sheath potentials [9]. A first attempt to characterise these heat loads was reported in [10], we shall here describe a more elaborate thermal model of the tiles subjected to local ICRF heat loads. The so called RF hot spots are located in the shadow of the poloidal limiters surrounding the antennae, and there is some evidence that they correspond to locations where a deposit has developed throughout the operation of JET. In particular, such deposit can be seen on pictures of the tiles taken during the 2010 shutdown (see Fig.2). Moreover, the time constant associated with temperature increase/decrease of the RF hot spots when turning ON/OFF the local ICRF power is short. This can hardly be explained by thermal models of the tiles without introducing a layer of material with poor thermal conductivity at the surface of the component. A simple way to model the thermal response of a tile with a deposit is using a 1D modelling as is sketched in Fig.3. This 1D approach is justified because the thickness of the deposit is small in comparison with the dimension of the heat pattern. The thermal diffusion equation is solved numerically using a finite difference scheme, in a plate including a bulk characterised by  $(x_{\text{bulk}}, \kappa_{\text{bulk}}, \rho_{\text{bulk}}, C_{\text{bulk}})$  and a thin deposit characterised by  $(x_{\text{depos}}, \kappa_{\text{depos}}, \rho_{\text{depos}}, C_{\text{depos}})$ , where  $x$  is the material thickness,  $\kappa$  is the thermal conductivity,  $\rho$  is the mass density, and  $C_p$  is the specific heat capacity. The deposit layer can also be characterised by the reduced quantities:

$$\tau_{\text{depos}} = (x_{\text{depos}} \times \rho_{\text{depos}} \times C_{p_{\text{depos}}}) / \alpha_{\text{depos}} \text{ and } \alpha_{\text{depos}} = \kappa_{\text{depos}} / x_{\text{depos}}$$

$\tau_{\text{depos}}$  is the characteristic thermal response time of the deposit (typical response time  $\sim 2$  s or less), and  $\alpha_{\text{depos}}$  is the deposit thermal conductance similar to the one defined in [11]; in quasistatic conditions, the temperature increase across the deposit is proportional to the heat flux:  $\Delta T_{\text{depos}} = Q / \alpha_{\text{depos}}$ . To take into account the real 3D properties of the CFC tile, we have run ANSYS<sup>TM</sup> reference simulations of the thermal response of the tile (without deposit). Then, in the 1D model without deposit, we have adjusted the bulk physical properties, with ad-hoc  $(x_{\text{bulk}}, \kappa_{\text{bulk}}, \rho_{\text{bulk}}, C_{p_{\text{bulk}}})$  parameters in order that the 1D bulk temperature response when exposed to a flux of  $1\text{MW}/\text{m}^2$  reproduces well the ANSYS modelling with the tile exposed to the same flux intensity (typical response time  $\sim 5$  s, see Fig.3 and Fig.4). Once the bulk properties of the 1D model are set, the only ‘free’ parameters that can be adjusted are  $\tau_{\text{depos}}$  and  $\alpha_{\text{depos}}$ ; they are adjusted so that the modelled temperature response when the tile is cooling down matches well the measured surface temperature assuming that the applied flux is null when the ICRF power is OFF. It is important to realise that the long time scale cooldown of the tile (typically  $\sim 5$ s) is essentially determined by the bulk properties and the flux intensity applied during the heating period while the fast cool down of the tile is function of  $\tau_{\text{depos}}$ ,  $\alpha_{\text{depos}}$  and of the applied heat-flux intensity; therefore the absolute heat flux evaluated using this modelling does not critically depends on the fine details of the deposit properties.

Rather, it will depend on the boundary conditions considered in the ANSYS reference simulations (adiabatic condition or fixed temperature of the back face, the size of the heat pattern, etc). These different boundary conditions lead to  $\pm 20$  % uncertainty in the intensity of the estimated heat fluxes. In figure 5, we show an example of heat-flux determination using this thermal model and the

deconvolution procedure described in section 2. When ICRF power is applied, the estimated heat flux varies between 0.35 and 0.6MW/m<sup>2</sup>, the cause of these oscillations is still under investigation. When ICRF power is turned-off, the estimated flux is null, and the good correspondence between the estimated and measured surface temperature is an indication of the quality of our thermal model. The deposit parameters used in this modelling are  $\tau_{\text{depos}} = 1.75\text{s}$  and  $\alpha_{\text{depos}} = 2.10^3\text{Wm}^{-2}\text{K}^{-1}$ . If we assume that the physical properties of the deposit are close to those of pyrolytic graphite ( $\rho_{\text{graph}} \sim 2.2 \times 10^3\text{kgm}^{-3}$ ,  $C_{p_{\text{graph}}} \sim 1.6 \times 10^3\text{JK}^{-1}\text{kg}^{-1}$ ), one can deduce from this model  $x_{\text{depos}} \sim 1\text{mm}$ , which agrees well with recent measurements of deposits with a few mm thickness on A2 septum tiles removed from JET during the 2010 shut-down. Finally we note that the value  $\alpha_{\text{depos}} \sim 2.10^3\text{Wm}^{-2}\text{K}^{-1}$  deduced from our analysis is compatible with the analysis of the thermal response of Tore-Supra CFC components with deposits [8]. Further, we have applied this analysis method to determine the heat flux on Antenna A septum location ‘A’ (see Fig.1), in a series of L-mode pulses in which only the following parameters were changed from pulse to pulse: power balance between antennae A&B versus C&D (the total ICRF power was kept to 3MW, A and B are fed from the same generators through a power splitter arrangement) - antenna-separatrix distance and thus electron density right at septum position - strap phasing. Fig6 summarises our findings: The heat-flux on A2 septum tiles increases linearly with the electron density at the septum position and with the RF voltage in the transmission lines feeding the antenna. This is consistent with simple models of power dissipation through RF sheaths rectification [9], and with some previous characterisation of the associated heat loads on Tore-Supra [13] and JET [10]. Also, current drive strap phasing leads to higher power dissipation. In general, strap phasing corresponding to lower // wave numbers ( $k_{//}$ , // refers to the direction parallel to the magnetic field) lead to higher heat fluxes in accordance with antenna modelling showing enhanced  $E_{//}$  (// component of the antenna electric field) in these cases [14].

#### 4. HOT SPOTS FROM LH ABSORPTION IN FRONT OF THE LAUNCHER

LH absorption in the SOL is explained by Electron Landau Damping of the waves with high  $N_{//}$  ( $N_{//} = k_{//}/k_0$ ) the components ( $|N_{//}| > 15$ ) directly in front of the grill, generating fast electrons in co and counter current directions with energies up to few keV [16]. This mechanism can explain the localised hot spots observed experimentally, and precisely located on JET components magnetically connected to the launcher [17]. Referring to Fig.9, and depending on the plasma configuration and LH launcher radial position, LH hot spots can be observed on the septa of A2 antennae A or B (location 1 and 4), ILA poloidal limiters (2 and 3), main poloidal limiter (5), upper dump plates (6), inner (7) and outer divertor aprons (8), with in some cases connection length of few tens of metres. FIG. 7 illustrates that fast electrons accelerated in front of the launcher rows will create a pattern of hot spots, corresponding to the projection of the launcher rows on the poloidal limiter, following the field lines. A thermal model of the LH hot spot on the ILA limiter-2 tiles (where a well defined hot-spot pattern can be observed) was developed via 3D finite element simulations with ANSYS™. A representation of this model is shown in Fig.8. The intensity of heat-flux normal to the surface is non uniform in the radial (x), vertical (y) and toroidal (z) directions.

The heat-flux has the following spatial dependence:  $Q(x,y,z) = Q_0 [\cos(y/7.2)]^2 \cdot f(x,z)$ , where  $y$  is in cm ( $y=0$  is the centre of the tile). This  $y$  dependence of the heat flux corresponds to the pattern of the electric field  $E_z(y)$ , in front of the waveguides of the LH launcher (see Fig.7), assuming that the fast electrons leaving the LH Launcher have energy proportional to  $|E_z(y)|^2$  consistent with the theory of LH wave absorption in front of the launcher [19]. The radial extension of the electron beam intercepting the limiter,  $x$ , is estimated from the grill position relative to the one of reference pulses (with same plasma configuration) when the hot spots ‘start’ appearing on the ILA limiter. The  $(x,z)$  dependence of the normal flux on the tile surface reflects the increase of the grazing angle of the field lines on the tile profile when going toward increasing  $z$ , and assuming that electron beam intensity is uniform along  $x$  (coherently with [17]). An example of analysis of the bottom hot spot on the ILA limiter is presented in Fig.10 (a) for Pulse No: 77393 in which LHCD is used between 6s and 12s, and the grill is retracted in 1 cm steps at 8s and 10s (radial grill position in front of the main poloidal limiter indicated in Fig.10 (b)). The LH grill fast electron beams generated from the 4 bottom rows of the grill is intercepted by the ILA limiter only for the retracted position (10-12s).

Applying the surface temperature deconvolution procedure on the bottom hot spot, local peak heat-flux has been calculated assuming that  $\Delta x = 7.5\text{mm}$ . The // heat flux plotted in Fig.10 (a) is evaluated taking into account the grazing angle of the field lines on the tile. At  $t=11\text{s}$ , it is in the range  $9\text{-}17\text{MW/m}^2$ . The error bars account for the uncertainty in the exact value of  $x$  ( $5\text{mm} < \Delta x < 10\text{mm}$  in this case). The heat flux on the ILA limiter tiles continuously increases during the exposure period. This could be caused by small changes of the field line incidence on the tiles, small changes of the grill position, or changes of SOL conditions ( $n_{e,\text{SOL}}$ ,  $T_{e,\text{SOL}}$ ) throughout the LH phase. As in this plasma configuration the fast electrons accelerated in front of the grill which are not intercepted by the poloidal limiter hit the upper dump plates, an independent evaluation of // heat flux associated with these electrons was also carried-out analysing the temperature evolution of the upper dump plates (Fig.10 (b)). Averaged on the hot-spot line connected to the bottom rows of the grill, the heat flux on the dump plates is  $\sim 0.05\text{MW/m}^2$ , which corresponds to a heat flux parallel to the field lines projected onto the plasma mid-plane of approximately  $10\text{MW/m}^2$ , and taking into account a flux expansion of 150 evaluated from 3D field line tracing based on the EFIT equilibrium code. Therefore, ILA limiter thermal analysis and dump plates analysis give, within uncertainties, equivalent heat fluxes estimates. For the LHCD system operation, it is important to determine the main parameters influencing the LH electron beam power density. Fig.11 represents a series of pulses with identical plasma conditions and in which we only varied the LH power in the 4 upper rows; the estimated heat flux onto the upper dump plates is plotted as a function of LH power density at the launcher, averaged in front of the active waveguides,  $\rho_{\text{LH}}$ . The heat flux intensity varies roughly as  $\rho_{\text{LH}}^2$ . This non-linear behaviour is compatible with Tore-Supra results [20], taking into account neutral ionization right in front of the grill leading to a local increase of the electron density and temperature [21] with LH. In two particular pulses in Fig.11, the same  $1.33\text{MW}$  is launched. Using fewer active waveguides (magenta square) and thus working at higher LH power density leads to a noticeably more intense fast electron beam.

## CONCLUSIONS

When using ICRF at JET, the large temperature increase observed in the vicinity of antennae is caused by rather low heat fluxes onto a deposit with low thermal conductance at the tile surface. In worst case conditions (1.5MW/antenna, current drive phasing, plasma- limiter distance of  $\sim 4$ cm) the observed heat-flux from ICRF interaction with SOL plasma on the A2 antenna septa is  $\sim 2\text{MW/m}^2$  (heat-flux along field lines  $\sim 5\text{MW/m}^2$ ). It will be important to confirm this analysis with the new wall which will be (at least at the beginning of the operations) free of deposit. The LH waves can accelerate electrons in the SOL creating very localised heat loads on PFCs magnetically connected to the grill. The maximum power density along the field lines associated with the LH fast e- beam is evaluated in the range  $15\text{--}30\text{MW/m}^2$  in the mid-plane. The maximum measured peak heat flux projected on tile surface was  $Q_0 \sim 7\text{MW/m}^2$  in worst case conditions ( $\rho_{\text{LH}} > 20\text{MW/m}^2$ , large fraction of the fast e- beam intercepted by limiter tiles). Such heat loads could be a problem for the Be wall if running long pulses but they can easily be mitigated by adjusting the launcher radial position and/or (if possible) plasma geometry so that fast e- are intercepted at small grazing angle. Heat-flux estimates must be taken with caution, as IR measurement errors and uncertainties in thermal models could lead to important errors; a more detailed discussion on this matter will be presented in an extended paper. The new Be tiles have been designed to sustain the equivalent of a flux of  $6\text{MW/m}^2 \times 10\text{s}$  projected on the surface. Therefore, care will be taken when operating JET with the ITER-like wall: to ensure ICRF and LH operation that preserves the Be wall integrity, a protection system including a new viewing system, real time detection of hot spots and real time control of ICRF or LH power is currently being developed.

## ACKNOWLEDGEMENTS

This work, part-funded by the European Communities under the contracts of Association between EURATOM and CCFE, CEA and other associations listed within the author list, was carried out within the framework of the European Fusion Development Agreement. The views and opinions expressed herein do not necessarily reflect those of the European Commission. This work was also part-funded by the RCUK Energy Programme under grant EP/G003955.

## REFERENCES

- [1]. M. Bures, et al., *Plasma Physics and Controlled Fusion* **33** No. 8 pp 937-967 (1991)
- [2]. J. Mailloux, et al., *Journal of Nuclear Materials* **241-242** p745 (1997)
- [3]. C.E. Thomas Jr, et al., *Journal of Nuclear Materials* **220-222** p531 (1995)
- [4]. G. F. Matthews, et al., *Physica Scripta* T138 014030 (2009)
- [5]. E. Gauthier, et al., *Fusion Engineering and Design* **83** 1335-1340 (2007)
- [6]. A. Kaye, et al., *SOFE Conf. Proc.*, 16th IEEE/NPSS Symposium, Vol. 1 p736 (1995)
- [7]. M. Goniche, et al., *Nuclear Fusion* **38**, 919 (1998)
- [8]. J.-L. Gardarein, et al., *Fusion Engineering and Design* **83** pp 759-765 (2008)
- [9]. F. W. Perkins, et al., *Nuclear Fusion* **29** No.4 pp.583-592 (1989)

- [10]. L. Colas, et al., in RF Power in Plasmas, AIP Conf. Proc. 1187 , pp 133-136 (2009)
- [11]. P. Andrew, et al., Journal of Nuclear Materials **313–316** (2003) 135–139
- [12]. ANSYS™ , ANSYS Inc., Canonsburg, PA 15317, USA.
- [13]. L. Colas, et al., Nuclear Fusion **46**, pp. S500-S513 (2006)
- [14]. V. Bobkov, et al., in RF Power in Plasmas, AIP Conf. Proc. 1187 , pp 221-224 (2009)
- [15]. J.-M. Noterdaeme, L.-G. Eriksson, M. Mantsinen, M.-L. Mayoral, D. Van Eester, J. Mailloux, C. Gormezano, T. T. C. Jones, Fusion Sc. and Tech. 53 1103-1151 (2008)
- [16]. V. Fuchs, et al., Physics of Plasmas **11** p. 4023 (1996)
- [17]. P. Jacquet, et al., in RF Power in Plasmas, AIP Conf. Proc. **1187** , pp 399-402 (2009)
- [18]. D. M. Pozar, Microwave Engineering (Addison-Wesley, Reading, MA, 1990)
- [19]. V. Fuchs, et al., Nuclear Fusion **43** pp 341-351 (2003)
- [20]. M. Goniche, et al., Plasma Physics and Controlled Fusion **46** (2004) 899–923
- [21]. M. Goniche, et al., Plasma Physics and Controlled Fusion **51** (2009) 044002 (18pp)

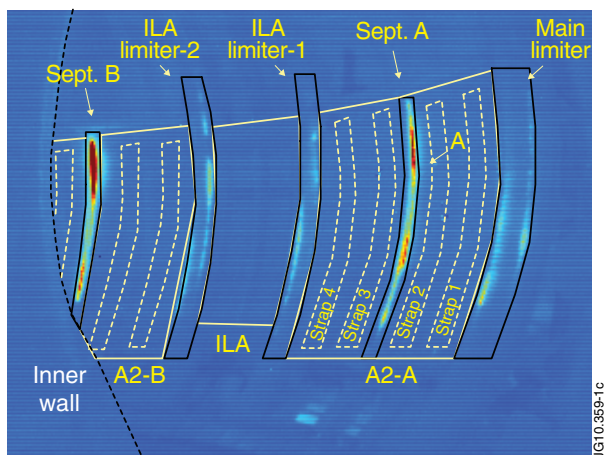


Figure 1: IR image, Pulse No: 79799,  $t = 23s$ . Superimposed are the A2 antennae A and half of B, the ILA antenna, the main and ILA poloidal limiters, and the A2 antenna septa. 'A' is the location where analysis of the surface temperature was carried-out. In this pulse, only A2 antennae A and B are used, launching 3MW.



Figure 2: Magnified photo of the plasma facing side of a septum tile from A2 antenna A. A deposit can be distinguished on the shadow of the tile.

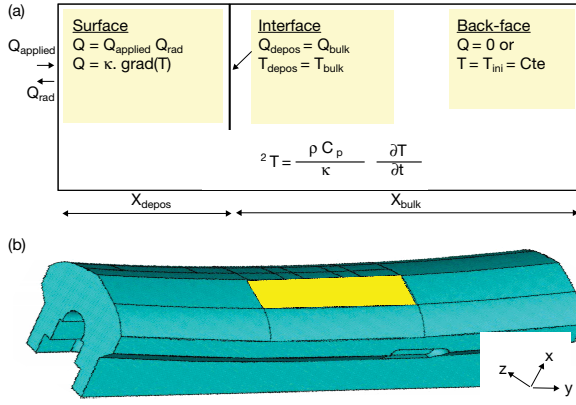


Figure 3: (a) Schematic of the 1D model including a deposit. The heat diffusion equation is solved numerically; boundary conditions are highlighted in yellow. (b) Schematic of a septum tile illustrating a reference ANSYS simulation. The heat flux pattern is applied on the yellow patch.

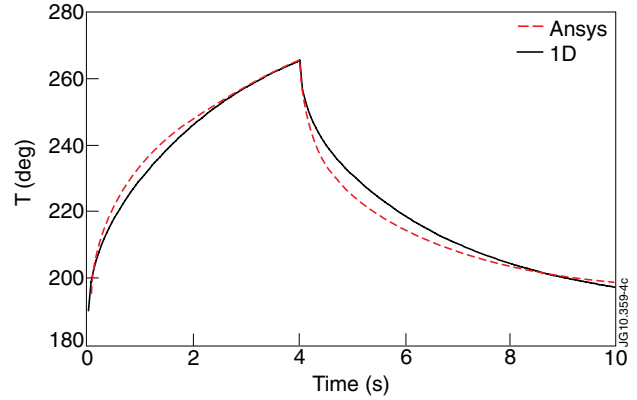


Figure 4: Time evolution of the tile surface temperature, comparison between ANSYS reference runs (surface temperature at center of hot spot) and the 1D-model of the bulk. The heat flux (1MW/m<sup>2</sup>) is applied between 0 and 4s.

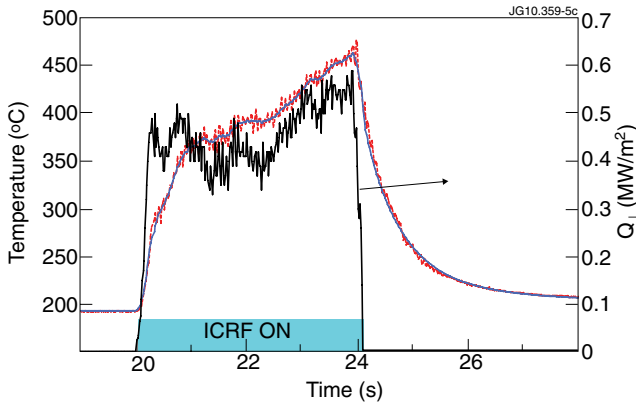


Figure 5: Pulse 79799 (3 MW from antennae A and B,  $\pi/2$  strap phasing). Heat flux at location 'A' from septum tile modelling including a deposit. IR measurement is in red, and the estimated flux is in black. When ICRF is OFF the flux is null and the estimated surface temperature (in blue) matches well the measurements, this is an indication of the good quality of the thermal model. This pulse is part of the series in FIG. 6 in which heat fluxes are averaged between 21s < t < 24s.

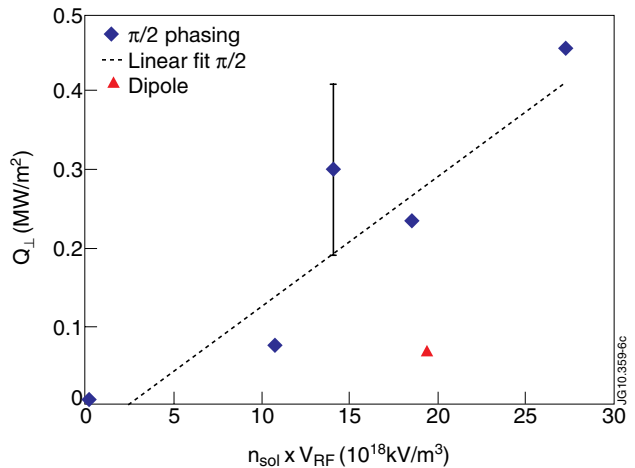


Figure 6: Flux at location 'A' versus the product of the SOL density and RF voltage. The SOL density from the edge reflectometer (not directly in front of the antenna) is taken at  $R=3.882\text{m}$  (position of limiters at midplane). The RF voltage (averaged over the 4 straps) is measured in the transmission lines feeding antenna A. The error bar is representative of the flux variation during RF.

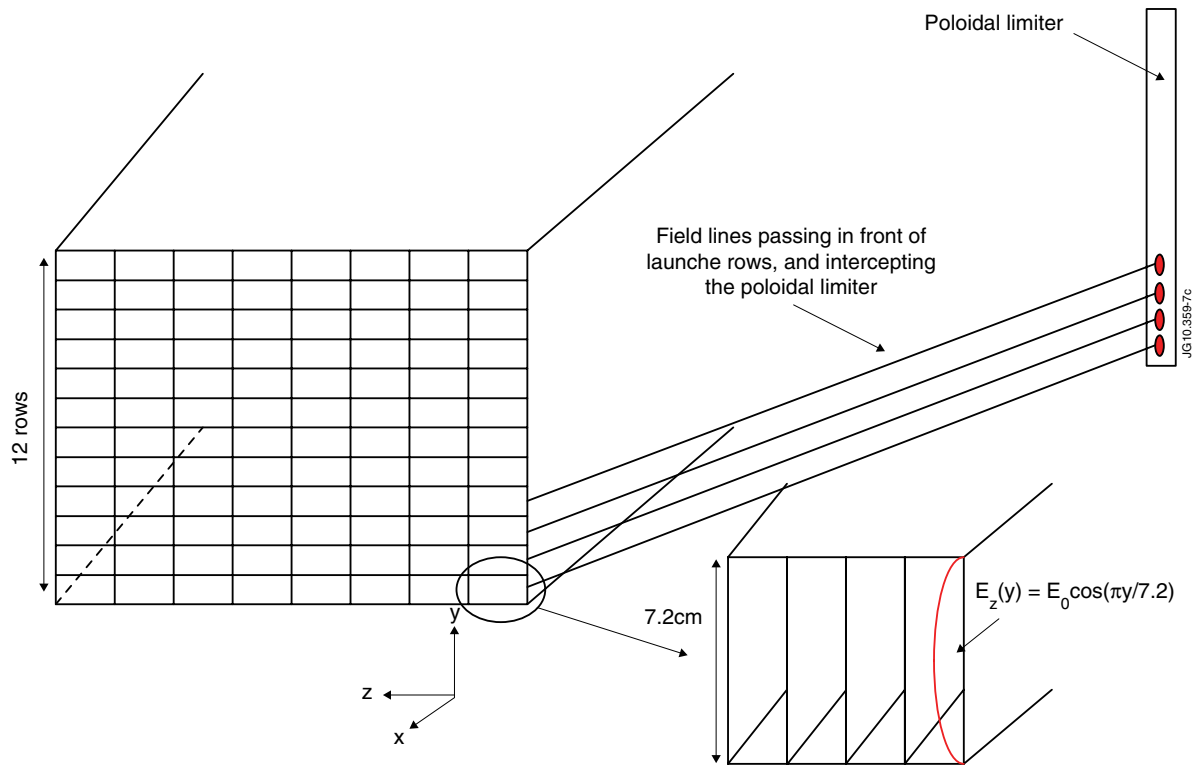


Figure 7: Illustration of LH hot spot formation on poloidal limiters. Hot spot pattern on the limiters is a projection of the grill rows, following the field lines leaving the grill. The  $E_z(y)$  electric field dependence corresponds to the  $TE_{1,m}$  and  $TM_{1,n}$  modes that can be excited at the waveguides aperture [18]. A description of the JET LH system can be found in [15].

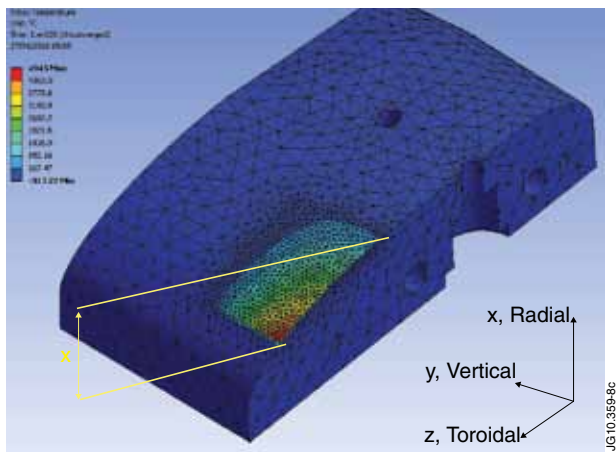


Figure 8: Thermal modelling of an LH hot-Spot on an ILA limiter tile with ANSYS. Half of the tile and of the hot spot is shown, vertical symmetry is assumed.  $x$  is the radial direction,  $y$  is the vertical direction, and  $z$  is the toroidal direction. CFC fibres are oriented in the  $(x,z)$  plan.

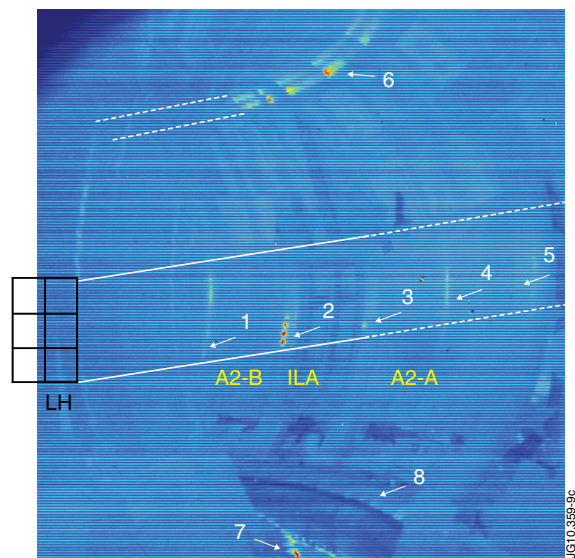


Figure 9: Pulse No: 77393  $t=12$  s, IR image showing where LH hot spots can be observed. The LH launcher is not viewed by the camera but its approximate location is shown. In this pulse the launched LH power density is  $\sim 24$   $MW/m^2$ , the top 4 rows and bottom 4 rows of the launcher are used. LH hot spots can be seen on the ILA poloidal limiter and on the upper dump plates.

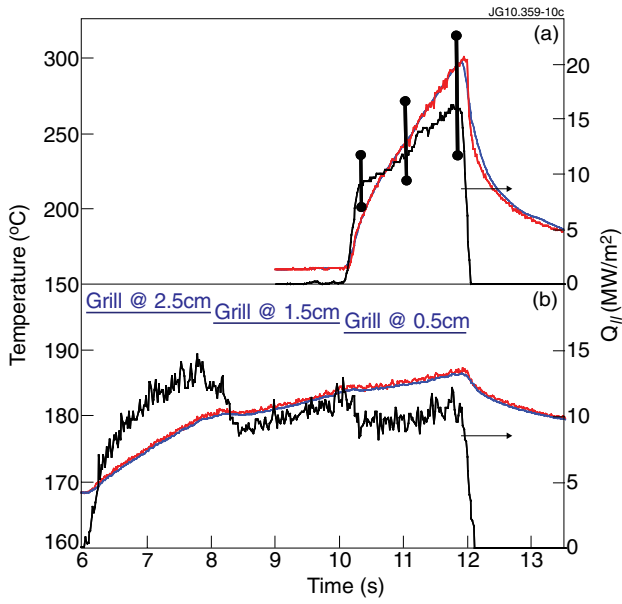


Figure 10: Pulse 77393. (a) Evaluation of the peak heat flux along magnetic field-lines associated with the bottom hot spot on ILA limiter. The evaluated heat flux is on the right y axis, and the measured (red) and evaluated (blue) temperatures are on the left y axis. (b) Heat flux along the field lines evaluated from the upper dump-plates temperature evolution, taking into account a flux expansion of 150 from plasma midplane toward the dump plates.

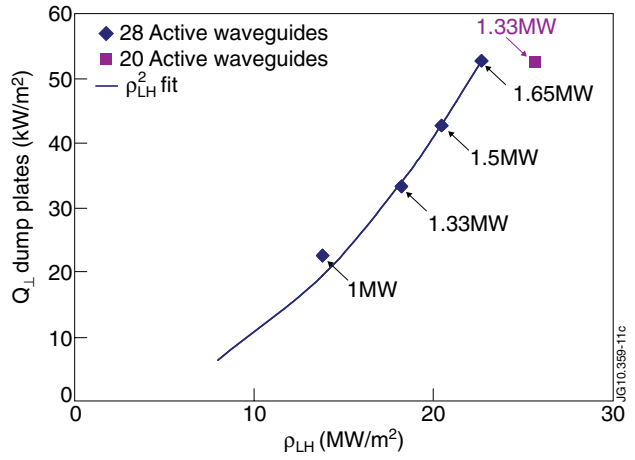


Figure 11: Heat flux on upper dump plates, from wave absorption in front of 4 top rows versus LH power density in active part of grill. Data from Pulse No's: 75736-75540, averaged between 8-9s. The labels indicate the total power launched from the 4 top rows.